



**CHALMERS**  
UNIVERSITY OF TECHNOLOGY

## **Single track versus bulk samples: Understanding the grain refinement in inoculated ferritic stainless steels manufactured by powder bed fusion-laser**

Downloaded from: <https://research.chalmers.se>, 2024-04-27 17:09 UTC

Citation for the original published paper (version of record):

Malladi, B., Chen, Z., Durga, A. et al (2023). Single track versus bulk samples: Understanding the grain refinement in inoculated ferritic stainless steels manufactured by powder bed fusion-laser beam. *Materialia*, 32(December, 2023). <http://dx.doi.org/10.1016/j.mtla.2023.101952>

N.B. When citing this work, cite the original published paper.



## Full Length Article

# Single track versus bulk samples: Understanding the grain refinement in inoculated ferritic stainless steels manufactured by powder bed fusion-laser beam

Sri Bala Aditya Malladi<sup>a</sup>, Zhuoer Chen<sup>a</sup>, A. Durga<sup>b</sup>, Niklas Holländer Pettersson<sup>b</sup>, Greta Lindwall<sup>b</sup>, Sheng Guo<sup>a</sup>, Lars Nyborg<sup>a</sup>

<sup>a</sup> Department of Industrial and Materials Science, Chalmers University of Technology, SE-41296, Gothenburg, Sweden

<sup>b</sup> Department of Materials Science and Engineering, KTH Royal Institute of Technology, Brinellvägen 23, SE-100 44 Stockholm, Sweden

## ARTICLE INFO

## Keywords:

Inoculation, Ferritic stainless steel, Powder bed fusion  
laser beam, Columnar to equiaxed transition, Single tracks

## ABSTRACT

One generic challenge in powder bed fusion - laser beam (PBF-LB) is the formation of epitaxially grown columnar grains, which lead to the undesirable anisotropy of mechanical properties. This anisotropy could be rectified by ex-situ or in-situ inoculation in some particular alloy systems. Understanding the grain refinement mechanism caused by in-situ inoculation is, however, complicated by remelting caused by the overlapping between neighboring scan tracks, when printing bulk samples using multiple tracks. Here in this work, a series of single tracks using ferritic stainless steels feedstock powder with and without pre-alloyed inoculant-forming elements, were printed at different scanning speeds to gain refreshed understanding on the mechanism of the observed grain refinement. Interestingly, the grain refinement in single tracks and bulk samples printed from the powder with and without inoculant-forming elements showed an opposite tendency. When using the powder without inoculant-forming elements, the single tracks showed large columnar grains, while the bulk samples showed even larger grain sizes; when using the powder with pre-alloyed inoculant-forming elements, fine equiaxed grains are found at the centers of the melt pools, surrounded by slightly coarser columnar grains at melt pool boundaries, in both single tracks and bulk samples. Noticeably, the mean grain sizes in the bulk samples are however smaller compared to those for single tracks because of remelting. Our work provides new insights on the grain refinement via in-situ inoculation during the PBF-LB process and highlights the importance of studying single tracks to better understand the melting and solidification behavior.

## 1. Introduction

Powder bed fusion - laser beam (PBF-LB) process is one of the various additive manufacturing processes, which utilizes high power laser to enable the fabrication of parts layer by layer. The use of high-power laser to rapidly melt and solidify thin layers of metal/alloy powder results in a unique hierarchical microstructure. However, this also results in high local thermal gradient ( $G$ ) and high liquid-solid interface velocity ( $V$ ) during solidification of each melt pool, which results in epitaxial growth of columnar grains spanning across a few layers, inducing the anisotropy of various properties with respect to the building direction [1–3].

It is possible to mitigate the columnar grain growth through the control of process parameters like laser power, scan speed, hatch distance, thereby influencing  $G$  and  $V$  to promote the columnar to equiaxed transition (CET). Also, the melt pool size and shape can be varied by process control to yield favorable microstructures, however, only to a

limited extent in terms of grain size control [4–6]. Increase in laser power and scan speed was reported to result in the grain size refinement in titanium, steel, aluminum, and cobalt alloys [7–10]. Still, grain refinement via changing process parameters is limited, as the process is bound by the processing windows of the materials using a given PBF-LB system, where a nearly full density of the part is mandated.

An alternative way to promote the CET is the introduction of secondary phase particles, i.e., inoculants which has been widely exploited in metal casting [11], to enhance heterogeneous nucleation within the melt pool. The efficacy of inoculation depends on several factors, namely lattice misfit, interfacial energy, melting point of the inoculant, size distribution and number density of the inoculants [11,12]. In the framework of the PBF-LB process, when using the powdered material, the addition of inoculating particles can be done either ex-situ or in-situ.

The ex-situ inoculation strategy uses powder mixtures of inoculants and the base metal powder. Martin et al. [13] added hydrogen-stabilized zirconium nucleants as precursors to the Al 7075 and 6065 aluminum

<https://doi.org/10.1016/j.mtl.2023.101952>

Received 10 July 2023; Accepted 31 October 2023

Available online 7 November 2023

2589-1529/© 2023 The Author(s). Published by Elsevier B.V. on behalf of Acta Materialia Inc. This is an open access article under the CC BY license (<http://creativecommons.org/licenses/by/4.0/>).

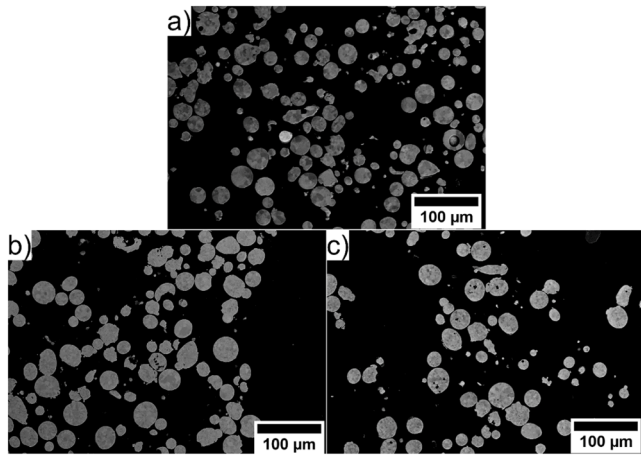


Fig. 1. Backscattered electron images of the a) Ti-free, b) SS441 and c) Ti-high pre-alloyed gas atomized powders.

alloys, which during solidification formed  $\text{Al}_3\text{Zr}$  to act as the inoculant to avoid solidification cracking by forming fine equiaxed grain structure in the as-printed condition. Xi et al. [14] reported the addition of  $\text{TiB}_2$  particles to aluminum alloys to result in the grain refinement and improved hardness, yield strength and ductility. Similarly, Kennedy et al. [15] reported that addition of TiN particles to Ti6Al4V resulted in the grain refinement. Li et al. [16,17] reported grain refinement by ex-situ addition of TiN particles to CoCrFeMnNi produced by PBF-LB. The ex-situ inoculation strategy, however, poses many challenges for the PBF-LB process. Firstly, a uniform mixture of inoculant and base metal powder of different size distributions is required to achieve consistent grain refinement throughout the PBF-LB parts. Secondly, the inoculant nanoparticles can agglomerate to form larger sized cluster during the melting and solidification process, which prevents effective grain refinement by reducing the number of nucleation sites available during solidification.

In the in-situ inoculation strategy, instead, the trace elements are pre-alloyed with the feedstock powder in for example the atomization process forming inoculants during the melting and solidification processes of PBF-LB to promote CET. Ikehata et al. [18,19] fabricated Fe-Ti alloys by PBF-LB under argon and nitrogen atmosphere, resulting in the formation of cubic  $\text{Ti}(\text{O},\text{N})$  particles as inoculants and therefore achieving the grain refinement and improved mechanical properties. The current authors demonstrated in a previous work [20] that the grain refinement of PBF-LB processed ferritic steel through in-situ inoculation, where elements (titanium and nitrogen) that form the inoculants were added to the alloy powder in the atomization process. During the melting and solidification in PBF-LB, these elements then reacted to form TiN particles which act as inoculants to induce the grain refinement in ferritic stainless steels. Compared to ex-situ inoculation, in-situ inoculation is more efficient in terms of achieving more homogenous distribution of inoculating particles in the printed parts.

The efficacy of TiN as an inoculant for ferritic steels is particularly effective in promoting the heterogenous nucleation by inoculation of ferrites, because of the low lattice mismatch between  $\{111\}$  planes of TiN and  $\{110\}$  planes of ferrite and favorable interfacial energies required for the wetting [12,21–23].

In this study, in-situ inoculation during the PBF-LB processing of a

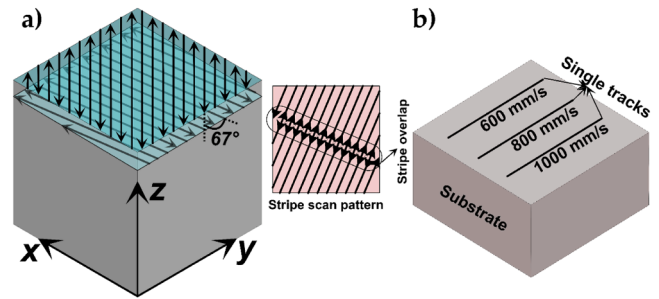


Fig. 2. Schematic showing the printing of a) bulk samples with x-y-z orientations,  $67^\circ$  scan rotation between layers, stripe scan strategy and b) single tracks printed on top of a substrate.

ferritic stainless steel is investigated with varying amounts of titanium in the pre-alloyed powder and varying process parameters (laser scan speed in this case). To distinctively reveal how the inoculants affect the formation of equiaxed or the columnar grains on the scale of melt pools, a single-track sample geometry is adopted by printing the tracks at different scan speeds and at constant laser power. Detailed analysis of the microstructure in the single tracks is undertaken, and the grain size and texture are evaluated in comparison to the counterpart bulk samples.

## 2. Materials and methods

Three different variants of alloys based on SS441[24] were used in this study with the main difference among them being the amount of titanium. The powder variants used in this study were gas-atomized in nitrogen atmosphere. The powder is spherical in shape and all variants were provided with particle sizes between  $15\text{ }\mu\text{m}$  and  $45\text{ }\mu\text{m}$ . The powder morphologies are illustrated in Fig. 1. The chemical compositions of the powder variants are shown in Table 1.

The PBF-LB experiments were conducted using an EOS M100 machine equipped with a 200-Watt Yb fiber laser with a spot diameter of  $\sim 40\text{ }\mu\text{m}$ . The build chamber was purged with argon gas prior to the start of the printing process, to maintain an oxygen level below 1000 ppm in the build chamber. The processing parameters for printing of bulk materials were previously optimized to achieve nearly full densities [20]. The set of optimized parameters include 110 W laser power, 800 mm/s scan speed,  $80\text{ }\mu\text{m}$  hatch distance and  $20\text{ }\mu\text{m}$  layer thickness. A striped laser scan pattern was employed using a stripe width of 5 mm and a stripe overlap of 0.1 mm, as illustrated in Fig. 2a. The scan vectors were rotated by  $67^\circ$  between subsequent layers for printing of bulk samples.

For printing of single tracks, unidirectional laser scans of 8 mm length were printed on top of substrates of the same material as of single tracks, with dimensions  $10\text{ mm} \times 10\text{ mm} \times 5\text{ mm}$ , as shown in Fig. 2b. The single tracks were produced with fixed laser power of 110 W and layer thickness of  $20\text{ }\mu\text{m}$ , but with varied scan speeds of 600 mm/s, 800 mm/s and 1000 mm/s. Each single-track sample contained ten layers in the build direction. The single-track experiments were conducted for all three alloy variants.

The printed bulk samples were sectioned parallel to building (hereafter referred as x-z orientation) and scanning directions (hereafter referred as x-y orientation). Both the sectioned bulk samples and single-track (in both x-z and x-y orientations) samples were then hot mounted in conducting resin. The mounted samples underwent metallographic

Table 1

Chemical compositions of the ferritic stainless steel powder variants used in this study in weight-percent (wt.%).

Material	Cr	Si	Mn	Nb	Ti	Ni	N	C	O	P	S	Fe
Ti-free	17.7	0.43	0.83	<0.01	<0.01	0.27	0.08	0.017	0.1	0.01	0.01	Balance
SS441	19.5	0.91	0.83	0.82	0.29	0.12	0.1	0.035	0.032	0.015	0.007	Balance
High-Ti	19.5	0.9	0.9	–	0.8	0.2	0.12	0.02	–	0.01	0.01	Balance

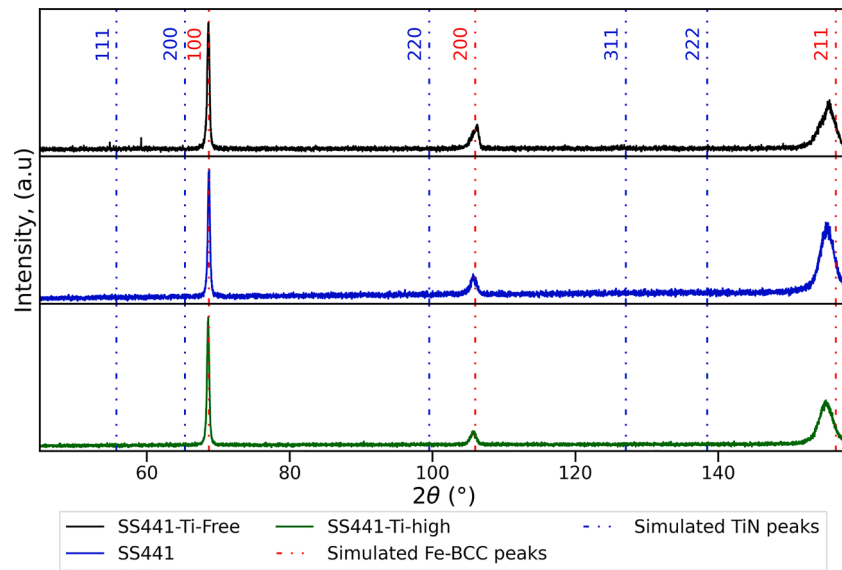


**Fig. 3.** X-Ray diffraction spectrum of the bulk Ti-free and Ti-containing samples in the as-printed state.

preparations first by grinding using 220 and 320 mesh SiC papers, followed by polishing using suspended diamond solutions of 9  $\mu\text{m}$ , 3  $\mu\text{m}$  and 1  $\mu\text{m}$  grit size in sequence. The final polishing of the samples was done using colloidal solution of 40 nm  $\text{SiO}_2$  particles to obtain mirror finish of the surfaces. The microstructure was examined using a Leo Gemini 1550 field emission gun scanning electron microscope (FEG-SEM). Energy dispersive X-ray spectroscopy (EDS) was performed to analyze the elemental composition using the Ultimmax detector by Oxford instruments. Automated particle analysis was performed at a magnification of 30,000X by combining the EDS data obtained from the point scans and morphological data obtained from the image analysis of the SEM images.

Electron back scattered diffraction (EBSD) was performed on both printed bulk samples and single-track samples using a Symmetry detector by Oxford Instruments. For acquisition of EBSD maps an acceleration voltage of 20 KeV was used, and a step size of 0.068  $\mu\text{m}$  was used

for the fine grain materials whereas a step size of 0.5  $\mu\text{m}$  was used for the coarse grain materials. The analysis of the EBSD data was performed using MTEX, an open-source MATLAB toolbox [25]. The X-ray diffraction (XRD) of printed bulk samples was performed using a Bruker AXS D8 Advance diffractometer equipped with a  $\text{Cr K}\alpha$  source ( $\lambda = 2.28970 \text{ \AA}$ ) operated at 35 kV and 40 mA.

### 3. Results

#### 3.1. Bulk samples

##### 3.1.1. X-ray diffraction

To identify the phases in the as printed samples, XRD analysis was carried out on all the three materials and the results are shown in Fig. 3. The observed peaks were indexed as BCC iron and no other phases were identified. Volume fractions of any other phases present could be too

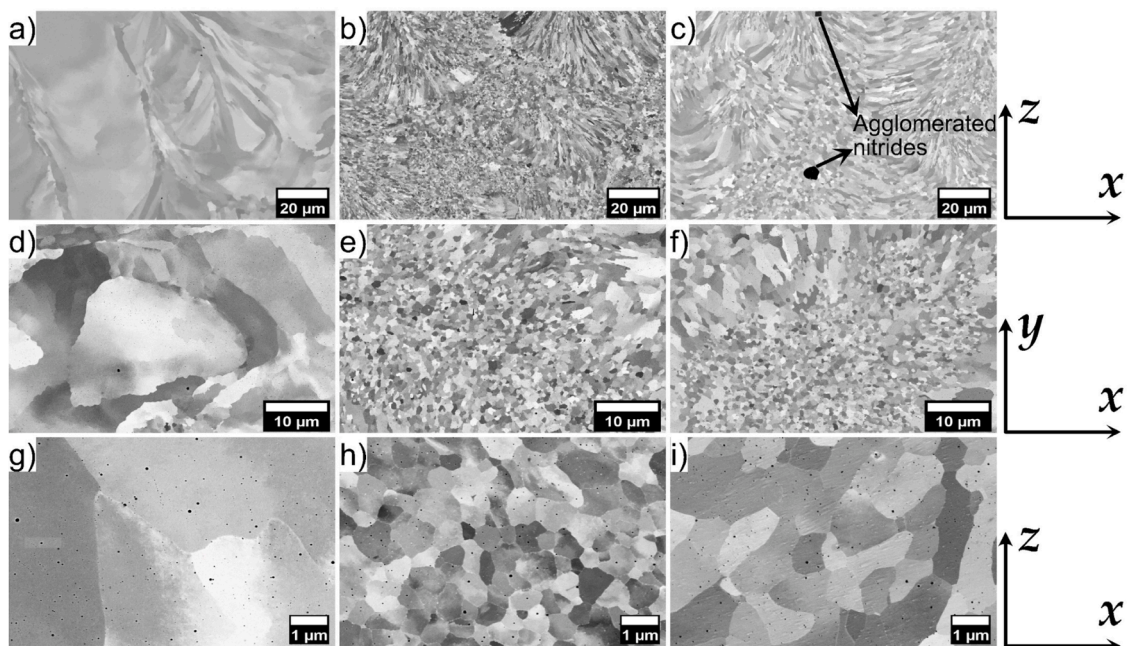


**Fig. 4.** BSE images of the Ti-free (a, d, g), SS441 (b, e, h) and the Ti-high material (c, f, i) in scanning and building directions of bulk samples, respectively.



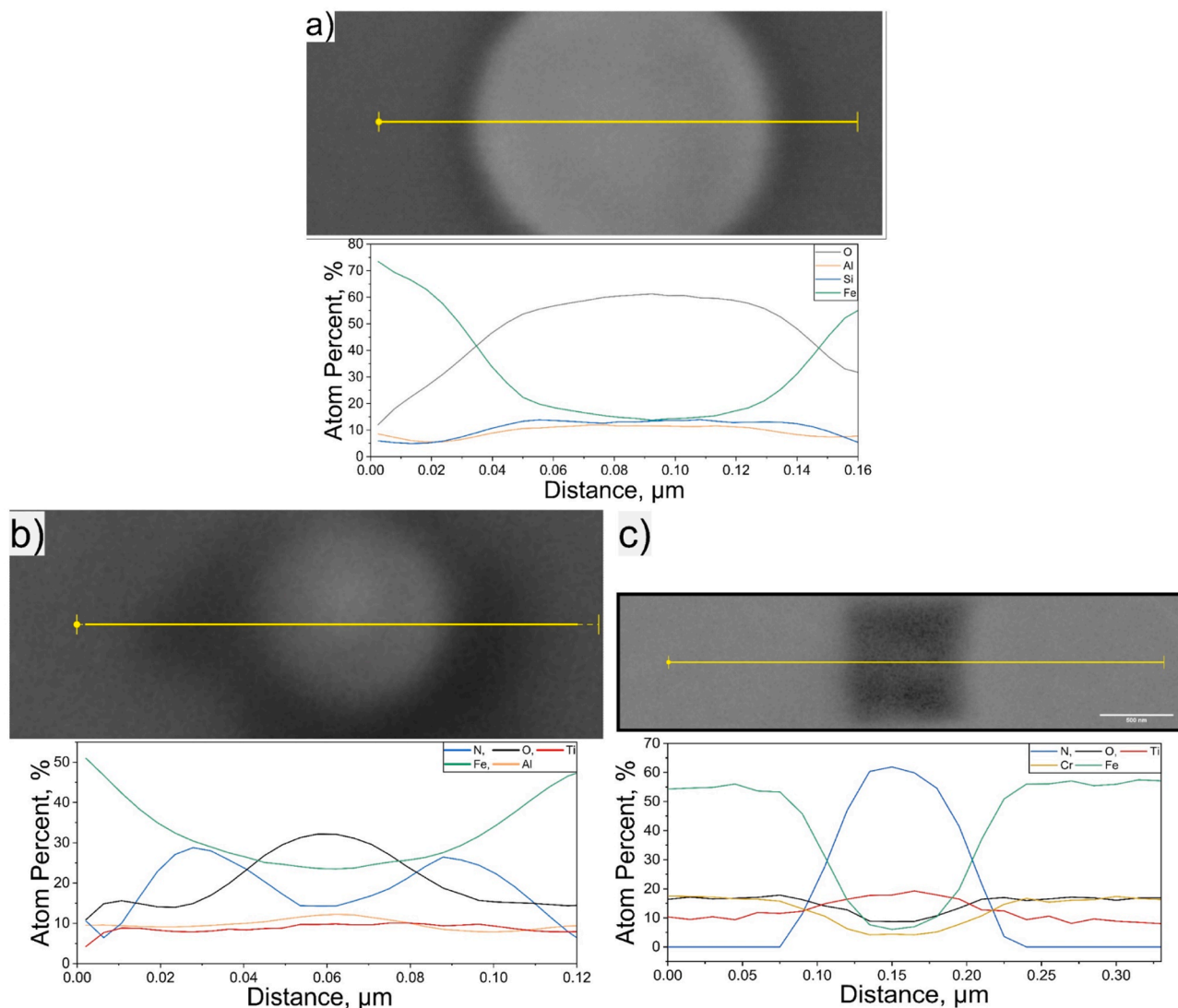


**Fig. 5.** EDS line scans of the particles showing a) Al-Si rich oxides in the bulk Ti-free material and b) core-shell structured oxy-nitrides and c) cuboidal shaped titanium nitrides in bulk Ti-containing materials.

small to be identified due to the resolution limit of XRD. Simulated XRD patterns of TiN and BCC-Iron were generated using the crystallographic information files (cif) and plotted using the python module pymatgen for Cr K- $\alpha$  wavelength overlaid on to the experimental data as shown in Fig. 3. The peak positions of (blue lines in Fig. 3) do not match with any of the three experimental peaks while the simulated peaks of BCC Iron (red lines in Fig. 3) do match with that of all the three observed peaks. This serves as a crucial validation, confirming that the crystallographic parameters of the material are close to those of the BCC Iron.

### 3.1.2. Microstructure of bulk samples

Fig. 4 shows the back-scattered electron (BSE) images at low and high magnifications of the bulk samples parallel to the build direction and perpendicular to building direction. A significant difference in the grain size between the Ti-free and the Ti-containing materials was observed. Epitaxially grown, large columnar grains were observed in the Ti-free material in the x-z and x-y orientation (Fig. 4a, d). This is consistent with the typical microstructure of materials manufactured using PBF-LB driven by the high local thermal gradient [8,26–30]. A mixture of fine, equiaxed grains and coarse grains were observed for both SS441 (Fig. 4b, e, h) and the Ti-high (Fig. 4c, f, i) material in both x-z and x-y directions. Closer observations at higher magnifications

revealed the different types of nano-sized particles distributed in the matrix of the Ti-free and Ti-containing materials (Fig. 4g, h and i). Finely dispersed spherical particles were observed for the Ti-free material whereas the mixture of spherical and cuboidal shaped particles was observed for both the Ti-containing materials, SS441 and the Ti-high material.

### 3.1.3. EDS of the particles and feature analysis

The particles found in the Ti-free, SS441 and the Ti-high samples were analyzed by means of EDS line scan to reveal their chemical compositions. The particles present in the Ti-free sample appear to be primarily Al-Si-containing oxides (Fig. 5a). SS441 showed two different types of secondary-phase particles. The first type of particles was found to be oxy-nitrides with core-shell structure, where the core appears to be Ti-Al rich oxide, while the shell is titanium nitride, see Figure 5b. The second type of particles were of cuboidal shape and were identified by EDS as titanium nitrides, see Fig. 5c. Like SS441, both the core-shell structured oxy-nitride particles and cuboidal shaped nitride particles were also observed in the Ti-high alloy. The mechanisms for the formation of these particles in both Ti-free and Ti-containing (SS441 and Ti-high) is discussed in detail in previous studies [20,24]

The Al-containing oxides that are present in all three variants of

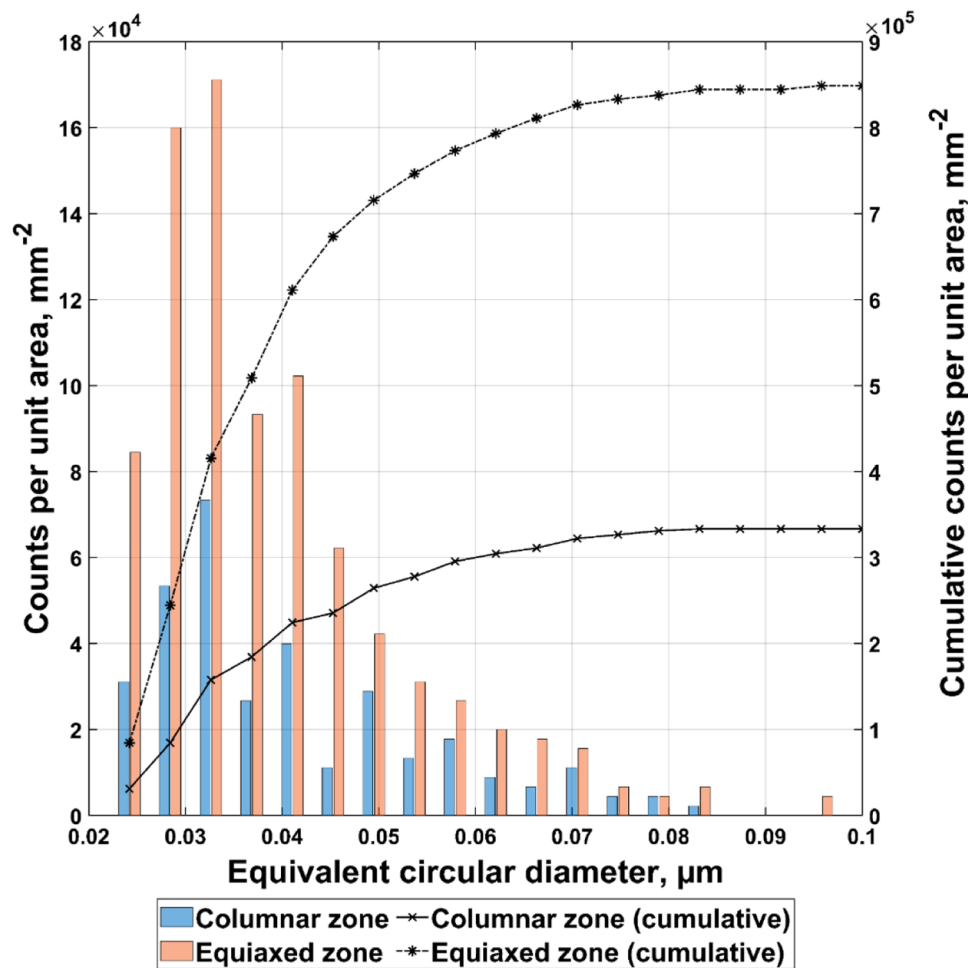


Fig. 6. Particle size distribution obtained from feature analysis in columnar and equiaxed regions of the bulk Ti-high material.

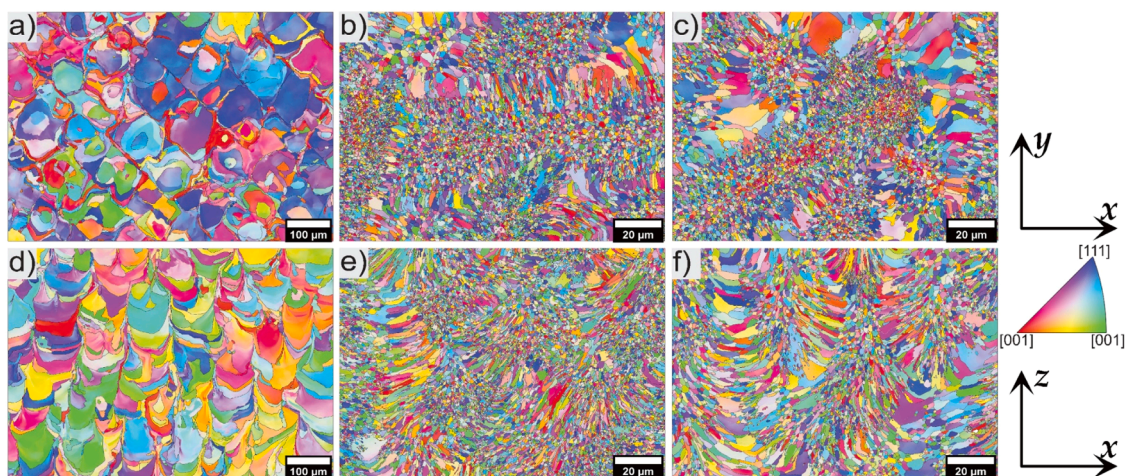
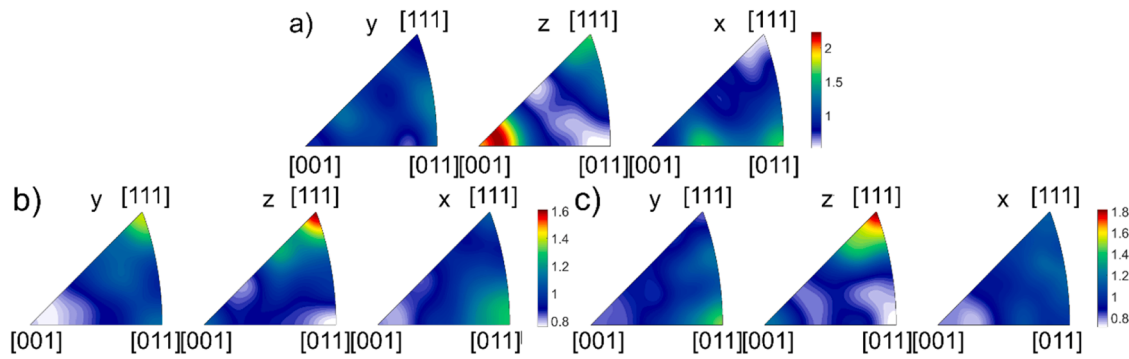


Fig. 7. EBSD orientation maps of bulk samples in the Ti-free material (a, d), SS441 (b, e) and the Ti-high material (c, f) in building and scanning directions, respectively.

materials did not serve as effective inoculants, since the Ti-free material that contains only such particles, showed a coarse and columnar grain structure (Fig. 4a, d, g). The pure nitrides and/or the core-shell structured oxy-nitrides have resulted in different extent of grain refinement in SS441 (Fig. 4b, e, h) and the Ti-high (Fig. 4c, f, i) material, as a mixture of columnar and equiaxed fine grains are observed. Based on the

inoculation theory, the size and number density of inoculating particles can significantly affect the grain refinement [11,31,32]. As shown in Fig. 6, for the Ti-high material, there are higher counts of nitride particles (both core-shell structured and cuboidal shaped as shown in Figs. 5b and 5c respectively), in the regions of equiaxed grains compared to the regions of columnar grains. The number density of nitride



**Fig. 8.** Inverse pole figures for the a) Ti-free material, b) SS441 and c) the Ti-high material computed from EBSD maps measured in the x-z planes of the bulk samples.

particles was measured to be  $\sim 0.89$  particles/ $\mu\text{m}^2$  in the regions of fine, equiaxed grain, which is 3 times higher than that in the regions of columnar grains ( $\sim 0.3$  particles/ $\mu\text{m}^2$ ). The average size of nitride particle in the columnar zone is  $39 \pm 16$  nm and in the equiaxed zone is  $38 \pm 21$  nm for both SS441 and the Ti-high alloys.

### 3.1.4. Bulk EBSD

Fig. 7 shows the EBSD orientation maps of the Ti-free material and the two Ti-containing materials in the x-y and x-z orientations. The Ti-free material showed a preferential orientation of the  $\{001\}$  lattice planes along the z-direction, whereas the Ti-containing materials showed preferential  $\{111\}$  orientation of lattice planes in the z-direction with lower overall texture intensities (Fig. 8). The number-weighted average grain sizes calculated from the EBSD maps in the x-z and x-y orientations (Fig. 7) are shown to be  $14.04 \pm 13.93$   $\mu\text{m}$  and  $9.98 \pm 11.13$   $\mu\text{m}$  for the Ti-free material,  $0.87 \pm 0.62$   $\mu\text{m}$  and  $0.94 \pm 0.68$   $\mu\text{m}$  for the SS441 sample,  $1.18 \pm 0.98$   $\mu\text{m}$  and  $0.93 \pm 0.72$   $\mu\text{m}$  for the Ti-high material, respectively. Hence, there is more than 10-fold decrease in average grain size for the two Ti-containing materials with inoculants compared to the Ti-free material.

### 3.2. Single tracks

It is not clear from the bulk samples where and how in the melt pool the grain refinement takes place, since the orientations of the melt pools are shifted from layer to layer due to the rotation of scan vectors. The single-track experiments were therefore designed and performed to better understand the mechanisms behind the formation of different grain morphologies in the Ti-free material and the Ti-containing materials. The ten layers in each single-track specimen were scanned by laser with the same orientation at the same positions. Thus, the melt pools are well aligned along the build direction. This allows for pinpointing the regions in which the small, equiaxed grains are formed with respect to the center and boundaries of the melt pools. In addition, the scan speed was varied while fabricating different single tracks to investigate its influence on the grain morphology.

The grains in the Ti-free single tracks are primarily columnar as one combines the views from both the horizontal planes and vertical planes in Fig. 9. The epitaxially grown columnar grains span across multiple powder layers, and there is no distinguishable melt pool boundary along the x-z orientation (Fig. 9d-f). The grains are columnar and curved towards the centerline of the single track. The grains at the centers of the single tracks are also columnar in nature but appear much narrower compared to the surrounding grains at the two sides. The increased laser scan speed induces instability in the scan track morphology and a reduction in track width. The number average grain size is also reduced because of the increased scan speed, from  $8.5$   $\mu\text{m}$  to  $7$   $\mu\text{m}$  along the building direction, or from  $8$   $\mu\text{m}$  to  $6$   $\mu\text{m}$  along the horizontal direction, when increasing the scan speed from  $600$  mm/s to  $1000$  mm/s.

It is clear from the single tracks of SS441 and the Ti-high material (Fig. 10 and Fig. 11) that the microstructure consists of a mixture of columnar grains and equiaxed grains. For both materials, there is also a clear pattern in the change in grain sizes and morphologies with respect to their locations in the melt pools: columnar grains originate from the melt pool boundaries and converge towards the center of the melt pools; fine, equiaxed grains appear at the center of the single tracks and bottoms of the melt pools. Near the top surfaces of the single tracks (the very last deposited layer of single track) there is a region of equiaxed grains with relatively coarser size. A thin layer of equiaxed grains appears near the side surfaces of the single tracks.

With other printing parameters being fixed, the varied scan speed changes the energy input to the single tracks and the melt pool dynamics, thus creating differences in the microstructure. At  $600$  mm/s scan speed, the melt pools are in the keyhole mode, featuring a large melt pool depth-to-width ratio. The keyhole melt pool shapes are clearly visible in both materials where the single tracks connect to the substrate (Fig. 10d and Fig. 11d). At the waists of the keyhole melt pools, the columnar grains are almost horizontally orientated. Increasing the scan speeds to  $800$  mm/s and  $1000$  mm/s, the melt pools become shallower, and the columnar grains are orientated at certain angles to the horizontal plane, featuring curved grain boundaries. In addition, with increasing scan speeds, the single-track morphology becomes unstable with large variations in track width as seen from both the x-y orientation (Fig. 10c and Fig. 11c) and x-z orientation (Fig. 10f and Fig. 11f).

## 4. Discussion

As shown from the results of this study, the presence of titanium and nitrogen in powder being processed in PBF-LB has a clear influence on the solidification and resulting grain morphology of the ferritic stainless steels. The mechanisms of the grain refinement by the titanium and nitrogen and the influence of scan speed on the grain refinement of the ferritic stainless steel studied are discussed below.

### 4.1. Mechanisms of grain refinement

The oxides formed/present evidently do not contribute to the inoculation, whereas TiN act as effective inoculants, as would be expected from the low lattice mismatch between TiN and ferrite matrix and the favorable interfacial energy [12,20,33]. As shown in Section 3.1.3, the three variants of materials contain different types of particles in as-built materials. The Ti-free material only contains oxides that are rich in aluminum and silicon, which do not seem to be effective inoculants. The other two materials with titanium in the feedstock powder exhibit significant grain refinement and show presence of TiN particles. During the melting and solidification process, titanium readily reacts with nitrogen to form TiN particles. Additionally, the oxides formed prior to the nucleation of the nitrides serve as the nucleation sites for TiN [23].



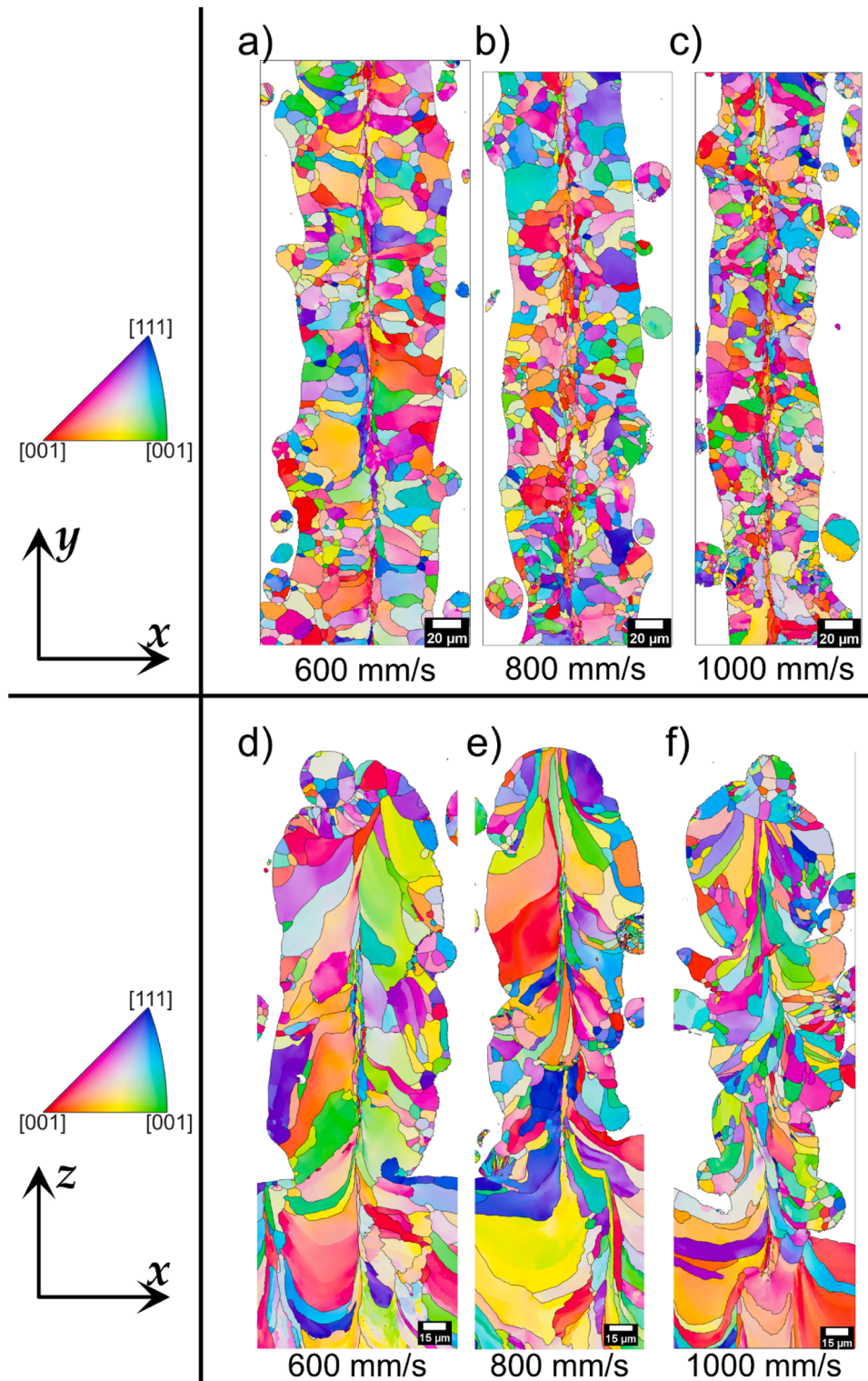


**Fig. 9.** EBSD orientation maps of the Ti-free single tracks in the x-y orientation a, b, c and in the x-z orientation d, e, f printed at 600 mm/s, 800 mm/s and 1000 mm/s, respectively.

It is necessary for the inoculants to grow to a critical size and constitute sufficiently high number density to promote effective grain refinement [34]. There are higher concentrations of TiN particles (with or without oxides in the core) in the equiaxed grain zone compared to in the columnar grain zone, as shown in Fig. 6, indicating a correlation between the inoculation effect and the size and number density of inoculating particles.

In the context of single melt pools, the equiaxed grains appear at the centers of the melt pools for the Ti-containing materials, while the columnar grains originate from the boundaries of melt pools towards the centerline. The formation of equiaxed, fine grains at the center of the melt pools might be the consequence of both the presence of effective inoculants and favorable solidification conditions. During the PBF-LB process, the centers of the melt pool experience longer liquid lifetimes



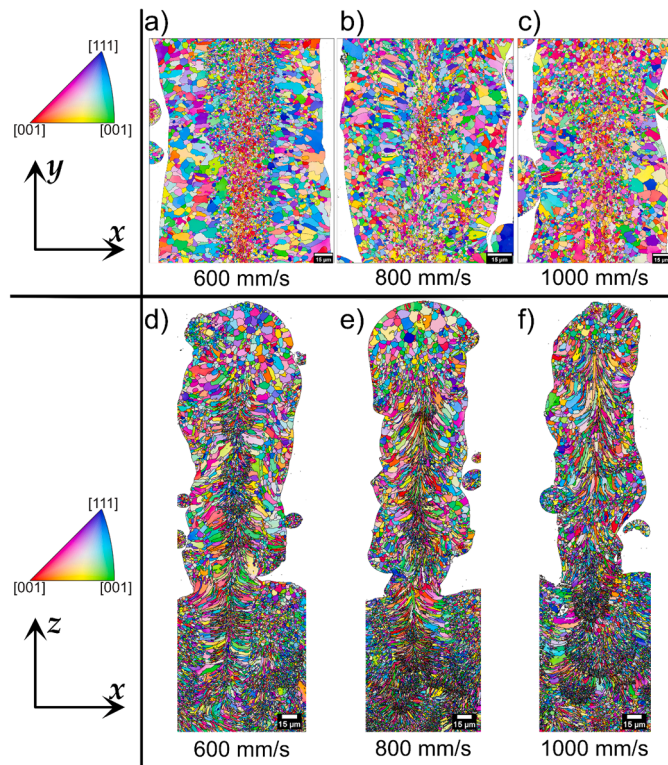


**Fig. 10.** EBSD orientation maps of the SS441 single tracks in the scanning direction a, b, c and in the building direction, d, e, f printed at 600 mm/s, 800 mm/s and 1000 mm/s, respectively.

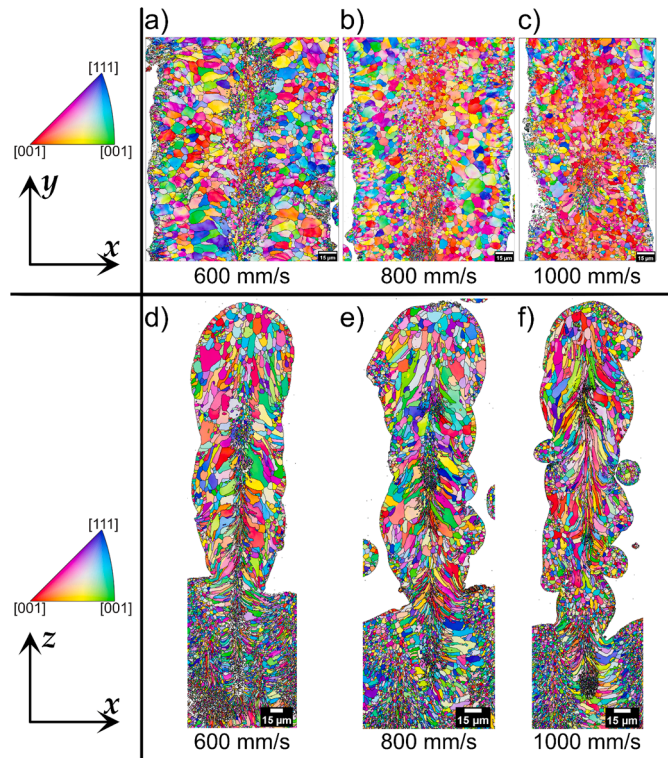


**Fig. 11.** EBSD orientation maps of the Ti-high single tracks in the scanning direction a, b, c of the image and in the building direction, d, e, f printed at 600 mm/s, 800 mm/s and 1000 mm/s, respectively.

compared to the edges of melt pools, allowing longer time for TiN

particles to nucleate and grow to reach critical size required for the inoculation effect during solidification. Also, it was reported that the varied solidification conditions ( $G$  and  $V$ ) from the center towards the boundaries of the melt pools can be responsible for the variations in grain structure [9,10]. During the solidification process, the center of the melt pool is supposed to experience lower thermal gradient  $G$  and higher velocity of solid-liquid interface  $V$  compared to the edges of the melt pools, which then favors the formation of equiaxed grains [35,36].

## 4.2. Implications of single-track study

### 4.2.1. Difference between bulk samples and single tracks in grain size distributions

Fig. 12 presents the grain size distributions of the single-track samples and bulk samples for the three materials under investigation. Evidently, the grain sizes measured from the bulk samples differ significantly from those measured from the single tracks. The origins of such differences between single-track samples and the bulk samples in grain size and microstructure are discussed below.

Firstly, the geometry of single-track samples naturally poses a strong influence of the side surface on the grain structure, which shifts the grain size distributions in single tracks towards opposite directions, as compared to those in bulk samples, in the Ti-free material and the Ti-containing materials. In the case of the Ti-free material, the grain sizes are much coarser in bulk samples compared to in the single tracks (Fig. 12a). The scan tracks have limited dimensions, which makes it impossible for a grain to grow in x-y orientation wider than half width of the scan tracks. While building bulk samples, the smaller grains near the free surfaces of the scan tracks would be remelted and transformed into coarser grains by neighboring scan tracks. The coarse columnar grains that span from the center of the melt pool to the side surfaces would also be remelted and grow sideways to become larger in size. Such epitaxial growth can be found at the connections between single tracks and the base material in Fig. 9d, e, and f.

In the case of SS441 and the Ti-high material, however, the grain size in the bulk samples is smaller than in the single track samples, contrary to the case of the Ti-free material. As seen in Fig. 10 and Fig. 11, the grains are finer towards the center of the melt pools in single tracks of both Ti-containing materials. While building bulk samples, the coarser grains at the edge of the melt pools are remelted and solidify into finer grains as they are close to the center of the overlapping melt pool. This results in larger areal fractions of fine grains in the bulk compared to the single-track samples, see Fig. 12b and c.

Secondly, the measurement of grain size through examinations of 2D cross-sections introduces a certain bias of the results. The grain sizes of the single tracks were measured from cross-sections that are either parallel to building direction (x-z plane) or perpendicular to the building direction (x-y plane). Knowing that grains are 3D objects and the columnar grains, in particular, possess certain orientation relationship with the building direction, such measurements would be biased due to the specific cross-sectioning. This is evidenced by the differences between the grain size distributions of single tracks measured in x-z plane and in x-y plane. This difference is most prominent for the Ti-free single tracks due to the dominant presence of columnar grains aligned with the building direction (Fig. 12a). By contrast, since the bulk samples were made with 67° scan rotations between layers, measuring the grain size from x-z orientation yields averaged results from grains in melt pools of various orientations relative to the cross-section.

Finally, the heat transfer conditions during the fabrication of single-track samples are different from fabrication of bulk samples with multiple hatches [37,38]. For single-track specimens, the first layer deposited was subjected to heat extraction by the base material and as the build progresses to the tenth layer the heat dissipation becomes gradually slower through the thin section underneath the current layer surrounded by powder with low effective conductivity. This leads to more equiaxed grains at the top of the single-track samples since the local

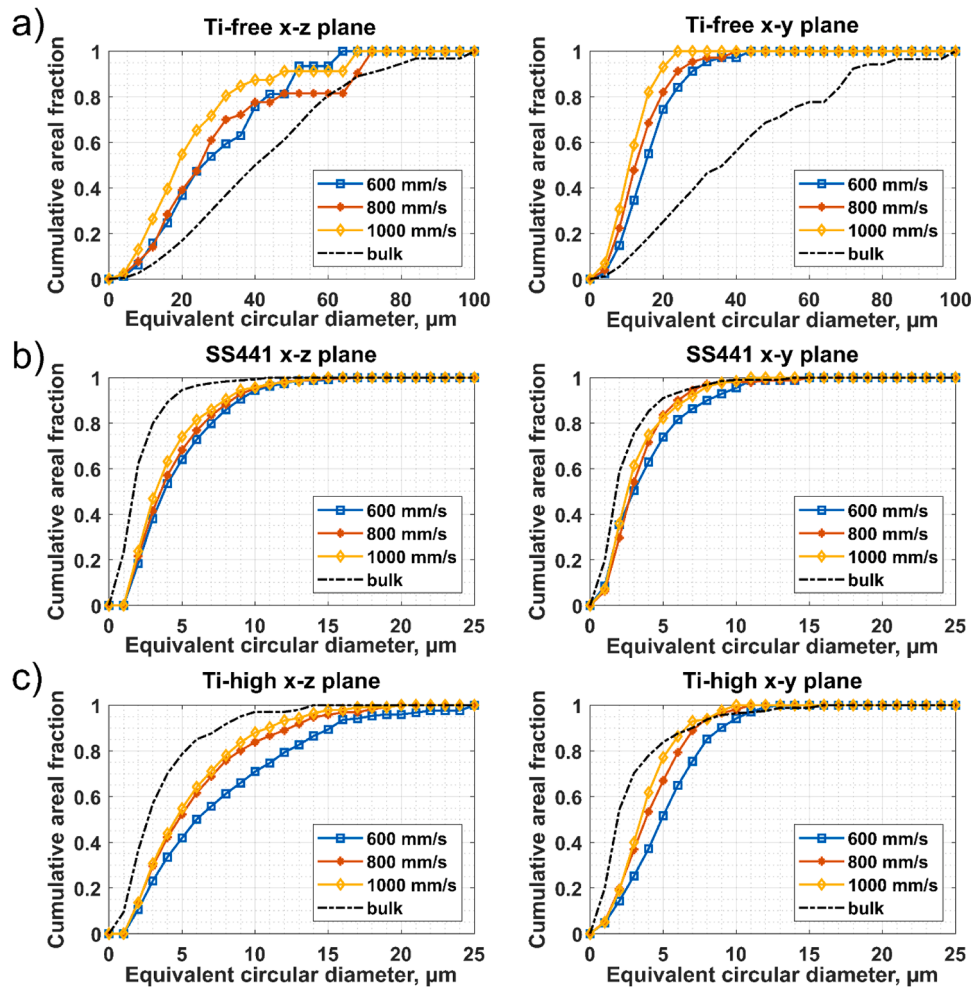


Fig. 12. Grain size distribution of single tracks and bulk samples in x-z and x-y planes for a) the Ti-free material b) SS441 and c) the Ti-high material.

thermal gradient is lower. The difference in thermal history can thus introduce microstructural differences between the bulk and single tracks.

#### 4.2.2. Sensitivity of grain size distributions to scan speed

Although implications cannot be directly drawn from the microstructure observations of single tracks for the bulk materials, the single tracks provide useful information regarding the inoculation effects on the scale of melt pools and the role of the varied scan speeds on the microstructure. For the Ti-free material, the grains are of finer sizes in single tracks produced with higher scan speed (Fig. 12a). Meanwhile, the increase in scan speed reduces the width of the single tracks, which limits the maximum size of grains as discussed previously. Nevertheless, the achievable grain refinement through manipulation of processing parameters is limited and the microstructure shows prevalent columnar grain growth.

On the other hand, the sample dimension is not a strongly limiting factor for grain growth in SS441 and the Ti-high material single tracks as the grain sizes are well below the dimensions of the samples. Hence, comparisons of grain size and morphology in the single-track samples can be made to infer the influence of the varied scan speed. For both SS441 and the Ti-high material single tracks, there is a small shift in grain size distribution towards the coarser size from 1000 mm/s to 800 mm/s and a larger shift from 800 mm/s to 600 mm/s scan speed (Fig. 12b and c). Compared to the Ti-high material, the grain size distributions in SS441 single tracks are observed to be less sensitive to the variations in scan speed. Since the size distribution curves in Fig. 12 are

plotted by areal fractions, the larger grains would have stronger influence on the distribution curve compared to smaller grains. From Fig. 12b and c, one can draw the conclusion that as the scan speed decreases there are higher area fractions of coarser grains (above  $\sim 2 - 3 \mu\text{m}$  where the three curves for single tracks starts to split). For the comparison of small grains, the reader is referred to the EBSD orientation maps in Fig. 10 and Fig. 11. With a lower scan speed, i.e., 600 mm/s, there are higher proportions of equiaxed, fine grains at the centers of the melt pools. This is conceivable since a lower scan speed increases the liquid lifetime at the center of the melt pool, which allows longer time for inoculating particles to nucleate and grow thus promoting CET.

## 5. Conclusions

In-situ inoculation during the PBF-LB process has proven to be effective for grain refinement in ferritic stainless steels. To better understand the grain refinement mechanism and in particular to generalize the inoculation effects in melt pools, the microstructure of single tracks printed using feedstock ferritic stainless steels powder with (Ti-containing) and without (Ti-free) pre-alloyed inoculant-forming elements, was studied and compared with that in counterpart bulk samples. Implications are drawn from the single tracks with considerations of the difference between single tracks and bulk samples in terms of geometrical effects and processing conditions. Noticeably, the grain refinement in single tracks and bulk samples printed from Ti-containing powder and Ti-free powder showed a completely opposite tendency. The main conclusions from the current works are as follows.



- 1 In the case of Ti-free single tracks, increase in scan speed from 600 mm/s to 1000 mm/s results in finer grains. The grains of the bulk samples of Ti-free material were much coarser compared to those in the single tracks, due to the epitaxial grain growth during the remelting by neighboring tracks and subsequent layers.
- 2 For both Ti-containing materials, fine, equiaxed grains with sizes under 1  $\mu\text{m}$  are highly concentrated at the center of the melt pools, whereas slightly coarser, columnar grains were found at the periphery of the fine equiaxed grain zone. This is attributed to the favorable solidification conditions (relatively low G, high V, and long liquid lifetime) at the centers of the melt pools for the nucleation and growth of inoculants, which is evidenced by the higher number density of titanium-nitride particles in the equiaxed grain regions.
- 3 For single tracks of Ti-containing materials, lower scan speed shifts the grain size distribution towards the coarser side by widening the melt pool and thus introducing higher fractions of coarser grains surrounding the center of melt pools. Meanwhile, lower scan speed also yields more equiaxed fine grains at the center of melt pools, by providing longer liquid lifetime for inoculants to nucleate and grow. However, this is a localized effect and does not alter the grain size distribution significantly. In the bulk samples, however, the overlapping between scan tracks increases the fractions of fine grains located at the center of scan tracks, therefore the overall grain size is finer in bulk samples as compared to isolated melt pools in the case of single tracks.

### Declaration of Competing Interest

The authors declare that they have no known competing financial interests or personal relationships that could have appeared to influence the work reported in this paper.

### Acknowledgements

This study was performed within the strategic innovation program Metalliska Material, one of the strategic innovation programmes of the Swedish Governmental Agency for Innovation Systems (Vinnova), Formas and Swedish Energy Agency, through the project Design of Novel Materials and Processes for Next Generation Additive Manufacturing (DEMA) (2018-00803) and the Competence Centre for Additive Manufacturing – Metals (CAM<sup>2</sup>) (2016-05175) with support from Vinnova. The industrial project partners Höganas AB, Kanthal AB, Quintus Technologies AB, Sandvik Materials Technology and Jernkontoret are acknowledged for valuable input. Roger Berglund, Kanthal AB, is acknowledged for materials supply, chemical analysis and valuable discussions.

### References

- [1] W.J. Sames, F.A. List, S. Pannala, R.R. Dehoff, S.S. Babu, The metallurgy and processing science of metal additive manufacturing, *Int. Mater. Rev.* 61 (2016) 315–360, <https://doi.org/10.1080/09506608.2015.1116649>.
- [2] S. Vunnam, A. Saboo, C. Sudbrack, T.L. Starr, Effect of powder chemical composition on the as-built microstructure of 17-4 PH stainless steel processed by selective laser melting, *Addit. Manuf.* 30 (2019), 100876, <https://doi.org/10.1016/J.ADDMA.2019.100876>.
- [3] W.E. King, A.T. Anderson, R.M. Ferencz, N.E. Hodge, C. Kamath, S.A. Khairallah, A. M. Rubenchik, Laser powder bed fusion additive manufacturing of metals; physics, computational, and materials challenges, *Appl. Phys. Rev.* 2 (2015) 41304, <https://doi.org/10.1063/1.4937809>.
- [4] M.J. Bermingham, D.H. StJohn, J. Krynen, S. Tedman-Jones, M.S. Dargusch, Promoting the columnar to equiaxed transition and grain refinement of titanium alloys during additive manufacturing, *Acta Mater.* 168 (2019) 261–274, <https://doi.org/10.1016/j.actamat.2019.02.020>.
- [5] J.P. Oliveira, A.D. LaLonde, J. Ma, Processing parameters in laser powder bed fusion metal additive manufacturing, *Mater. Des.* 193 (2020), 108762, <https://doi.org/10.1016/J.MATDES.2020.108762>.
- [6] J.A. Spittle, Columnar to equiaxed grain transition in as solidified alloys, *Int. Mater. Rev.* 51 (2006) 247–269, <https://doi.org/10.1179/174328006x102493>.
- [7] J.J. Marattukalam, D. Karlsson, U. Pacheco, P. Beran, U. Wiklund, U. Jansson, B. Hjörvarsson, M. Sahlberg, The effect of laser scanning strategies on texture, mechanical properties, and site-specific grain orientation in selective laser melted 316L SS, *Mater. Des.* 193 (2020), <https://doi.org/10.1016/j.matdes.2020.108852>.
- [8] A.B. Spierings, K. Dawson, T. Heeling, P.J. Uggowitzer, R. Schaublin, F. Palm, K. Wegener, Microstructural features of Sc- and Zr-modified Al-Mg alloys processed by selective laser melting, *Mater. Des.* 115 (2017) 52–63, <https://doi.org/10.1016/J.MATDES.2016.11.040>.
- [9] A.B. Spierings, K. Dawson, P.J. Uggowitzer, K. Wegener, Influence of SLM scan-speed on microstructure, precipitation of Al 3 Sc particles and mechanical properties in Sc-and Zr-modified Al-Mg alloys, *Mater. Des.* 140 (2018) 134–143, <https://doi.org/10.1016/j.matdes.2017.11.053>.
- [10] D.F. Louw, P.G.H. Pistorius, The effect of scan speed and hatch distance on prior-beta grain size in laser powder bed fused Ti-6Al-4V, *The Int. J. Adv. Manuf. Technol.* 103 (2019) 2277–2286, <https://doi.org/10.1007/S00170-019-03719-W>, 2019 103:5.
- [11] B.S. Murty, S.A. Kori, M. Chakraborty, Grain refinement of aluminium and its alloys by heterogeneous nucleation and alloying, *Int. Mater. Rev.* 47 (2002) 3–29, <https://doi.org/10.1179/095066001225001049>.
- [12] B.L. Bramfitt, The effect of carbide and nitride additions on the heterogeneous nucleation behavior of liquid iron, *Metall. Trans.* 1 (1970) 2958, <https://doi.org/10.1007/BF03037838>.
- [13] J.H. Martin, B.D. Yahata, J.M. Hundley, J.A. Mayer, T.A. Schaedler, T.M. Pollock, 3D printing of high-strength aluminium alloys, *Nature* 549 (2017) 365–369, <https://doi.org/10.1038/nature23894>, 2017 549:7672.
- [14] X.P. Li, G. Ji, Z. Chen, A. Addad, Y. Wu, H.W. Wang, J. Vleugels, J. van Humbeeck, J.P. Kruth, Selective laser melting of nano-TiB<sub>2</sub> decorated AlSi10Mg alloy with high fracture strength and ductility, *Acta Mater.* 129 (2017) 183–193, <https://doi.org/10.1016/J.ACTAMAT.2017.02.062>.
- [15] J.R. Kennedy, A.E. Davis, A.E. Caballero, S. Williams, E.J. Pickering, P. B. Prangnell, The potential for grain refinement of Wire-Arc Additive Manufactured (WAAM) Ti-6Al-4V by ZrN and TiN inoculation, *Addit. Manuf.* 40 (2021), 101928, <https://doi.org/10.1016/J.ADDMA.2021.101928>.
- [16] B. Li, B. Qian, Y. Xu, Z. Liu, F. Xuan, Fine-structured CoCrFeNiMn high-entropy alloy matrix composite with 12 wt% TiN particle reinforcements via selective laser melting assisted additive manufacturing, *Mater. Lett.* 252 (2019) 88–91, <https://doi.org/10.1016/j.matlet.2019.05.108>.
- [17] B. Li, L. Zhang, B. Yang, Grain refinement and localized amorphization of additively manufactured high-entropy alloy matrix composites reinforced by nano ceramic particles via selective-laser-melting/remelting, *Compos. Commun.* 19 (2020) 56–60, <https://doi.org/10.1016/J.COCO.2020.03.001>.
- [18] H. Ikehata, E. Jägle, Grain refinement of Fe-X alloys fabricated by laser powder bed fusion, *Mater. Sci. Forum.* (2021) 580–586, <https://doi.org/10.4028/WWW.SCIENTIFIC.NET/MSF.1016.580>, 1016 MSF.
- [19] H. Ikehata, E. Jägle, Evaluation of microstructure and tensile properties of grain-refined, Ti-alloyed ferritic stainless steel fabricated by laser powder bed fusion, *Mater. Sci. Eng.: A* 818 (2021), 141365, <https://doi.org/10.1016/J.MSEA.2021.141365>.
- [20] A. Durga, N.H. Pettersson, S.B.A. Malladi, Z. Chen, S. Guo, L. Nyberg, G. Lindwall, Grain refinement in additively manufactured ferritic stainless steel by in situ inoculation using pre-alloyed powder, *Scr. Mater.* 194 (2021), <https://doi.org/10.1016/j.scriptamat.2020.113690>.
- [21] W.J. Poole, A. Mitchell, F. Weinberg, Inoculating Stainless Steel with Titanium Nitride, *High Temp Mater. Process.* 16 (1997) 173–182, <https://doi.org/10.1515/HTMP.1997.16.3.173>.
- [22] M.-L. Wang, G.-G. Cheng, S.-T. Qiu, P. Zhao, Y. Gan, Roles of titanium-rich precipitates as inoculants during solidification in low carbon steel, *Int. J. Min., Metall. Mater.* 17 (2010) 276, <https://doi.org/10.1007/s12613-010-0305-9>.
- [23] J. Fu, Q. Nie, W. Qiu, J. Liu, Y. Wu, Morphology, orientation relationships and formation mechanism of TiN in Fe-17Cr steel during solidification, *Mater. Charact.* 133 (2017) 176–184, <https://doi.org/10.1016/J.MATCHAR.2017.10.001>.
- [24] D. Karlsson, C.Y. Chou, N.H. Pettersson, T. Helander, P. Harlin, M. Sahlberg, G. Lindwall, J. Odqvist, U. Jansson, Additive manufacturing of the ferritic stainless steel SS441, *Addit. Manuf.* 36 (2020), 101580, <https://doi.org/10.1016/j.addma.2020.101580>.
- [25] F. Bachmann, R. Hielscher, H. Schaeben, Texture Analysis with MTEX – Free and Open Source Software Toolbox, *Solid State Phenomena* 160 (2010) 63–68, <https://doi.org/10.4028/WWW.SCIENTIFIC.NET/SSP.160.63>.
- [26] X. Gong, K. Chou, Microstructures of Inconel 718 by Selective Laser Melting, in: TMS 2015 144th Annual Meeting & Exhibition, 2015, pp. 461–468, [https://doi.org/10.1007/978-3-319-48127-2\\_58](https://doi.org/10.1007/978-3-319-48127-2_58).
- [27] M.R. Rolchigo, M.Y. Mendoza, P. Samimi, D.A. Brice, B. Martin, P.C. Collins, R. LeSar, Modeling of Ti-W Solidification Microstructures Under Additive Manufacturing Conditions, *Metall. Mater. Trans. A* 48 (2017) 3606–3622, <https://doi.org/10.1007/S11661-017-4120-Z>, 2017 48:7.
- [28] S. Ghosh, L. Ma, L.E. Levine, R.E. Ricker, M.R. Stoudt, J.C. Heigel, J.E. Guyer, Single-Track Melt-Pool Measurements and Microstructures in Inconel 625, *JOM* 70 (2018) 1011–1016, <https://doi.org/10.1007/S11837-018-2771-X>, 2018 70:6.
- [29] X. Liu, C. Zhao, X. Zhou, Z. Shen, W. Liu, Microstructure of selective laser melted AlSi10Mg alloy, *Mater. Des.* 168 (2019), 107677, <https://doi.org/10.1016/J.MATDES.2019.107677>.
- [30] A. Basak, S. Das, Epitaxy and Microstructure Evolution in Metal Additive Manufacturing, *Annu. Rev. Mater. Res.* 46 (2016) 125–149, <https://doi.org/10.1146/annurev-matsci-070115-031728>.
- [31] A.L. Greer, J.H. Perepezko, F. Franks, B. Cantor, R.W. Cahn, Grain refinement of alloys by inoculation of melts, in: *Philosophical Transactions of the Royal Society A: Mathematical, Physical and Engineering Sciences*, Royal Society, 2003, pp. 479–495, <https://doi.org/10.1098/rsta.2002.1147>.

- [32] A.L. Greer, T.E. Quested, Heterogeneous grain initiation in solidification, *Philos. Mag.* 86 (2006) 3665–3680, <https://doi.org/10.1080/14786430500198486>.
- [33] K. Nakajima, H. Hasegawa, S. Khumkoa, S. Mizoguchi, Effect of a catalyst on heterogeneous nucleation in pure and Fe-Ni alloys, *Metall. Mater. Trans. B* 34 (2003) 539–547, <https://doi.org/10.1007/S11663-003-0022-0>, 2003 34:5.
- [34] J.D. Hunt, Steady State Columnar and Equiaxed Growth of Dendrites and Eutectic, *Mater. Sci. Eng.* 65 (1984) 75–83.
- [35] J.C. Villafuerte, H.W. Kerr, S.A. David, Mechanisms of equiaxed grain formation in ferritic stainless steel gas tungsten arc welds, *Mater. Sci. Eng. A* 194 (1995) 187–191, [https://doi.org/10.1016/0921-5093\(94\)09656-2](https://doi.org/10.1016/0921-5093(94)09656-2).
- [36] S. Kou, *Welding Metallurgy*, 3rd ed., Wiley, 2020 <https://doi.org/10.1002/0471434027>.
- [37] I. Yadroitsev, Ph. Bertrand, G. Antonenkova, S. Grigoriev, I. Smurov, Use of track/layer morphology to develop functional parts by selective laser melting, *J. Laser Appl.* 25 (2013), 052003, <https://doi.org/10.2351/1.4811838>.
- [38] I. Yadroitsev, P. Krakhmalev, I. Yadroitsava, S. Johansson, I. Smurov, Energy input effect on morphology and microstructure of selective laser melting single track from metallic powder, *J. Mater. Process. Technol.* 213 (2013) 606–613, <https://doi.org/10.1016/j.jmatprotec.2012.11.014>.